

## A mathematical model of blood, cerebrospinal fluid and brain dynamics

Andreas A. Linninger · Michalis Xenos ·  
Brian Sweetman · Sukruti Ponshe ·  
Xiaodong Guo · Richard Penn

Received: 13 June 2008 / Revised: 13 January 2009 / Published online: 15 February 2009  
© Springer-Verlag 2009

**Abstract** Using first principles of fluid and solid mechanics a comprehensive model of human intracranial dynamics is proposed. Blood, cerebrospinal fluid (CSF) and brain parenchyma as well as the spinal canal are included. The compartmental model predicts intracranial pressure gradients, blood and CSF flows and displacements in normal and pathological conditions like communicating hydrocephalus. The system of differential equations of first principles conservation balances is discretized and solved numerically. Fluid–solid interactions of the brain parenchyma with cerebral blood and CSF are calculated. The model provides the transitions from normal dynamics to the diseased state during the onset of communicating hydrocephalus. Predicted results were compared with physiological data from Cine phase-contrast magnetic resonance imaging to verify the dynamic model. Bolus injections into the CSF are simulated in the model and found to agree with clinical measurements.

**Keywords** Cerebrospinal fluid · Communicating hydrocephalus · Intracranial pressure · Mathematical modeling · Computational fluid dynamics

---

A. A. Linninger · M. Xenos · B. Sweetman · S. Ponshe  
Laboratory for Product and Process Design (LPPD),  
Department of Bioengineering and Chemical Engineering,  
University of Illinois at Chicago, Chicago, USA

A. A. Linninger (✉)  
Department of Bioengineering and Chemical Engineering, University of Illinois at Chicago,  
Science and Engineering Offices (SEO), Room 218 (M/C 063),  
851 S Morgan St, Chicago, IL 60607-7052, USA  
e-mail: linninge@uic.edu

X. Guo · R. Penn  
Department of Neurosurgery,  
University of Chicago, Chicago, USA

**Mathematics Subject Classification (2000)** 74F10 · 76Z05 · 92B05

### Abbreviations

cAr	Carotid artery
Ar	Arteries
Al	Arterioles
Cp	Capillaries
Vl	Veinules
V	Veins
vSinus	Venous sinus
Lv	Lateral ventricle
3V	Third ventricle
4V	Fourth ventricle
SAS	Cranial subarachnoid space
sp.canal	Spinal subarachnoid space
br	Brain
exf	Extracellular fluid
$xx^{L,R}$	Signifying two equations, one for the left brain hemisphere and one for the right brain hemisphere
$xx^R$	Right compartment
$xx^L$	Left compartment
$f_{xx_{in}}$	Flow into the compartment
$f_{xx_{out}}$	Flow out of the compartment

## 1 Introduction

### 1.1 Motivation

A variety of central nervous system diseases alter intracranial dynamics and changes in dynamics may in turn result in changes to the brain. An important example is hydrocephalus in which the cerebral ventricles enlarge, thus in effect displacing and compressing brain tissue. This condition is well described clinically, but its fundamental dynamic principles are poorly understood. The goal of our research is to provide such an understanding and by doing so point the way to new treatment based on this knowledge.

Current mathematical models do not incorporate the interaction between the cerebral vasculature, parenchyma and cerebrospinal fluid (CSF) during the cardiac cycle, and many models do not account properly for conservation of the fluid volume (Lakin et al. 2003; Sorek et al. 1988a). According to the Monro-Kellie doctrine, the cranium is a closed system, enclosing the *brain*, *CSF* and *cerebral blood*; but for intracranial dynamics to be described correctly the spinal canal and its pulsating CSF displacements need to be included. The flow of CSF with each cardiac pulse into and out of the spinal subarachnoid space is well known by clinicians and

has been measured by Cine phase-contrast MRI (Pelc et al. 1991; Loth et al. 2001; Raksin et al. 2003; Zhu et al. 2006). As we will show, it is critically important in accounting for CSF flow patterns inside the ventricular and subarachnoid systems.

## 1.2 Background

Some early models of the brain vasculature have simplified the dynamics by lumping numerous compartments (Sorek et al. 1988a,b, 1989; Ursino and Lodi 1997; Stevens 2000). Other approaches use bundles of tubes to represent different types of cerebral blood vessels (Zagzoule and Marc-Vergnes 1986). Monro's first model of the intracranial cavity consisted of two compartments, brain and blood. This model was expanded by Karni to contain several fluid structures, including arterial, capillary, venous, venous sinus, jugular bulb, and CSF pathways (Sorek et al. 1988a,b). To refine the model, Karni et al., added an additional component, brain tissue, to the previous six compartments model. Piechnik and collaborators developed a mathematical model to study autoregulation and cerebral species transport in the human brain (Piechnik et al. 2001). Marmarou derived a widely used mathematical model that describes intracranial pressure (ICP) dynamics (Marmarou et al. 1978). However, his model does not explicitly incorporate brain vasculature or the porous parenchyma in the calculations. Many researchers have based their experimental work on this model which correlates well with experimental data, but does not predict blood alterations or brain water content change (Czosnyka et al. 2004).

For the current study, a more complete dynamic model consisting of the bi-phasic brain, arteries, arterioles, capillaries, veinules, veins, venous sinus, ventricles, subarachnoid space and the spinal canal will be described and compared to experimental results obtained from Cine phase-contrast MRI measurements. This multi-compartment mathematical model accounts for cerebral hemodynamics, the expansion or compression of the parenchyma and the CSF flow dynamics. The expansion of the vasculature is linked with the volumetric change of the brain parenchyma. In turn, changes in cerebral volume affect the space available to the ventricles and the CSF. Due to the full coupling of the distensible blood vessels, CSF spaces, and the brain parenchyma, it is possible to solve dynamic force and mass balances of the entire system. The model is used to simulate normal and pathological conditions to determine the temporal change in ICPs and volumes for the various brain structures. The brain parenchyma pressure is a function of the force interaction with the embedded cerebral vasculature and CSF. Hence, elevation of ICP is not an input to the model, but is calculated by solving the model equations for the brain interacting with CSF and blood. Similarly, ventricular expansion is only possible as a function of force balances and flow equations. The objective is to describe and quantify the dynamic interactions between blood flow, ICP, extensions of the cerebral vasculature and brain parenchyma during the cardiac cycle, and how it is changed in pathological conditions. The modeling results should consistently describe the transient force interactions between blood, CSF and brain. Predictions of accurate states are a secondary objective.

**Table 1** Comparison of maximum CSF flow velocity at prepontine area and junction between the aqueduct of Sylvius, AS, and fourth ventricle, 4V

	Average peak to peak flow velocity at prepontine (mm/s)	Average peak to peak flow velocity at AS and V4 (mm/s)	Average peak to peak flow velocity ratio (Prepontine/AS and V4)
Normal CSF ( $N_N = 6$ )	$37.06 \pm 12.21$	$6.91 \pm 3.95$	5.36
Communicating Hydrocephalus ( $N_{HC} = 5$ )	$19.35 \pm 7.11$	$23.56 \pm 19.69$	0.82

### 1.3 Outline

The methods section describes the MRI techniques and acquisition of experimental data. Section two introduces the mathematical equations describing blood and CSF flow as well as the equations for fluid and solid motion in the bi-phasic parenchyma. Results are presented in section three for normal intracranial dynamics and their validation with experimental MRI measurements. The pathological conditions of communicating hydrocephalus are predicted qualitatively and quantitatively. We show the use of standard clinical tests like a bolus injection to determine brain parameters, and compare results with previously published experiments in section four (Czosnyka et al. 2004, 2002, 2005). Section five discusses our new mechanistic explanation of hydrocephalus, its implications, and the limitations of current models.

## 2 Methods

### 2.1 Measuring ICP in dog brains

Prior experiments with dogs were conducted to establish whether pressure gradients exist between the ventricles, brain tissue and subarachnoid space in acute or chronic hydrocephalus (Penn et al. 2005). The outcome of these experiments showed that no transmante pressure differences between the ventricles and subarachnoid space could be detected in any of the dogs before kaolin administration or afterwards when hydrocephalus developed.

### 2.2 Cine phase-contrast MRI in the human brain

CSF flow velocity vectors were determined in eleven subjects, six normal and five with hydrocephalus, in several regions of interest using a Cine phase-contrast MRI technique. These velocity vectors were measured over the cardiac cycle using simultaneous gating (Pelc et al. 1991; Dumoulin et al. 1988) on a 3T GE Signa scanner, GE Medical Systems, Milwaukee, WI. The data acquisition and velocity calculation we used have been discussed elsewhere (Zhu et al. 2006). Experimental results are summarized in Table 1.

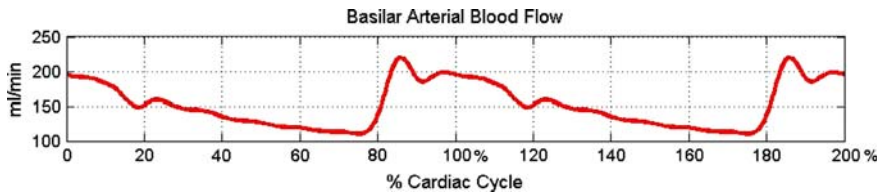


**Fig. 1** MRI was used to measure the blood flow in the basilar artery (ml/min) as a function of the cardiac cycle (100% = 1 beat). The basilar artery signal was represented with discrete Fourier series of seventeen coefficients:  $c_0 = 102.3530$ ;  $a_1, \dots, a_8 = (-0.0345, -0.0511, -0.0267, -0.0111, -0.0013, 0.0050, 0.0027, 0.0061)$ ;  $b_1, \dots, b_8 = (0.1009, 0.0284, -0.0160, -0.0070, -0.0174, -0.0041, -0.0041, 0.0005)$

Size changes of the lateral ventricle were also determined by MRI. The axial slice with the largest size of the lateral ventricles was used. The edge between brain tissue and lateral ventricle was drawn based on  $T_2$ - or  $T_1$ -weighted images. This drawing marks the initial pixel positions during a full cardiac cycle. The position-shift of each pixel at the edge of the lateral ventricle is then estimated for each time frame of the cardiac cycle by integrating the velocity over time. The edge points of the lateral ventricle at each cardiac time frame were connected by spline interpolation (de Boor 2001). The area change of the enclosed region was then calculated by comparison with the time-averaged area of this enclosed region throughout the cardiac cycle assuming that the lateral ventricle changes its size uniformly. The total lateral ventricle volume change was estimated based on the  $T_1$ -weighted volume images, after conversion of voxel dimensions to milliliters (Zhu et al. 2006).

Cine phase-contrast MRI was also used to measure the timing of the arterial pulse wave; with mean blood pressure of 100 mmHg absolute. Figure 1 displays the MRI measurements of blood flow in the basilar artery (ml/min) (Zhu et al. 2006). Table 1 provides a comparison of the aqueduct of Sylvius and fourth ventricle flow velocity and the prepontine flow velocity in normal and hydrocephalic subjects scanned with the Cine phase-contrast MRI technique. These measurements were used as a reference for the predictions of the mathematical model of intracranial dynamics.

### 2.3 Mathematical model of intracranial dynamics

In order to better understand the dynamic forces linking CSF with blood motion, a *multi-compartment dynamical model of intracranial dynamics* was designed. The model accounts for the force interaction of three principal elements—the cerebral vasculature, the CSF pathways and the bi-phasic brain parenchyma. Blood is modeled as viscous and incompressible fluid flowing through the *cerebral vasculature*, which is divided into arteries, arterioles, capillaries, venules, veins and venous sinus. The *CSF system* includes the lateral, third and fourth ventricles, cerebral and spinal subarachnoid spaces which are all connected. The *brain parenchyma*, divided in two hemispheres, is treated as a bi-phasic medium composed of extracellular fluid and a solid cell matrix. The network of intracranial compartments and their connectivity is depicted in Fig. 2. All compartments, except the spinal subarachnoid space, are enclosed inside the cranium. The *Monro-Kellie doctrine* of constant cranial volume

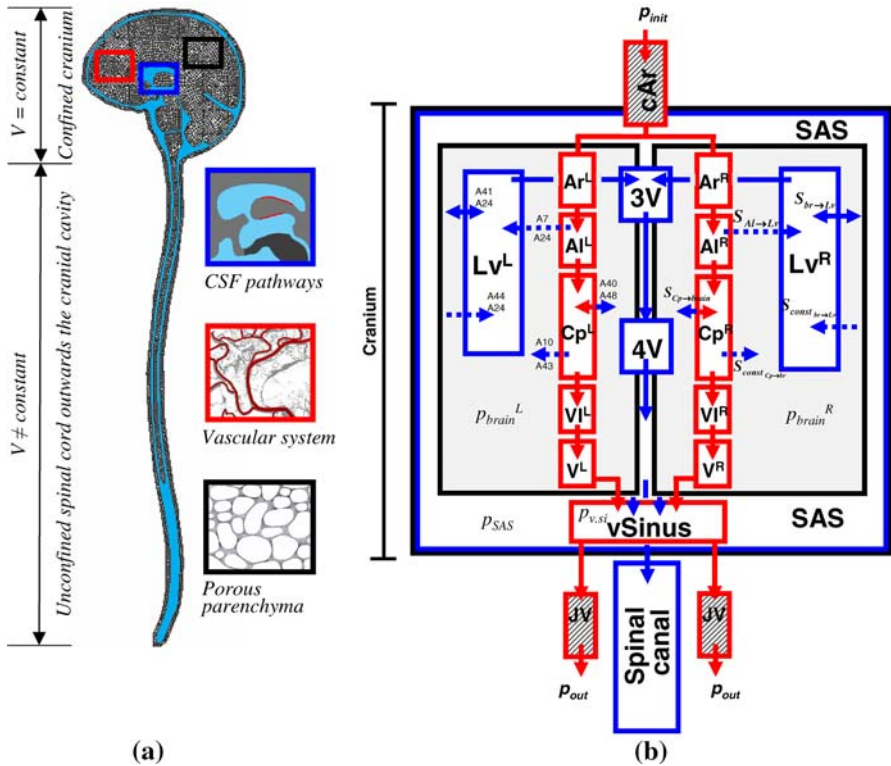


**Fig. 2** **a** The proposed holistic model is composed of three main layers inside the cranial vault—the *ventricular system*, the *cerebral and spinal subarachnoid space*, *blue*, where CSF flows, the *vascular system*, *red*, where blood flows; and the *parenchyma*, a bi-phasic medium with extracellular fluid motion and constant solid cell matrix, *black*. **b** The main blood compartments are the carotid artery, *cAr*, main arteries, *Ar*, arterioles, *Ar*, capillaries, *Al*, capillaries, *Cp*, veinules, *Vl*, veins, *V*, venous sinus, *vSinus*, and jugular veins, *JV*. The CSF system is composed of the lateral ventricles, *Lv*, third and fourth ventricles, *3V*, *4V*, subarachnoid space, *SAS*, and the *spinal canal* outside of the cranium. The parenchyma is divided into the right and left hemisphere, indicated by superscript, *L/R* for individual compartments. The arterial pressure in the carotid is  $p_{init}$ ; the venous pressure in the jugular vein is  $p_{out}$ . The ICP in the parenchyma is  $p_{brain}^{L/R}$ , and  $p_{v.si}$  is the venous sinus pressure. Mass transfer fluxes between compartments are indicated by labels carrying the equation number with prefix *A* found in the Appendix. Other mass transfer terms  $S_{I \rightarrow II}$  describing fluid source and sink terms are explained in Sect. 2. *Dashed arrows* indicate CSF production, while *solid arrows* signify pressure driven fluid exchange (color in online)

is enforced rigorously. However, CSF can be displaced into the expandable spinal subarachnoid space which is not confined by the skull bone.

Fluid flow in our model is governed by the pressure difference between the carotid arteries and the jugular veins (Fig. 2). The model contains one main artery as input, labeled *cAr*. The carotid pressure signal,  $p_{init}$  is displayed in Fig. 3c,  $P_{init}$ . This signal was based on Cine phase-contrast MRI measurements of a normal subject and was used as a dynamic boundary condition in the model; it was fitted using discrete Fourier series consisting of 17 coefficients enumerated in Fig. 1.

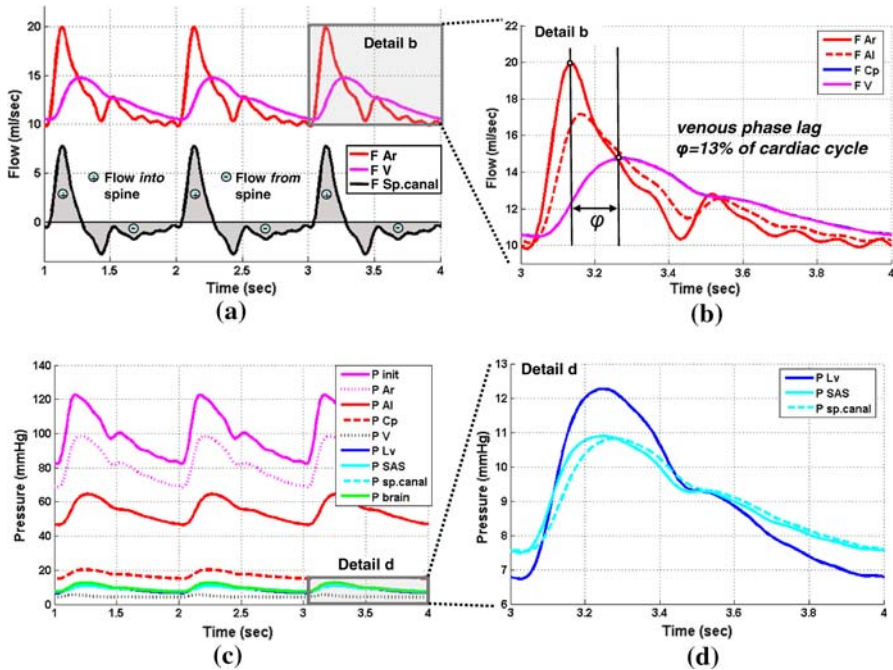


**Fig. 3** Simulated normal intracranial dynamics for an individual with a carotid blood pressure of 120/80 mmHg. **a** The flow in the vascular system (arteries, arterioles, capillaries, venules, veins and venous sinus) has a mean value of 12.3 ml/s. The forward volume at each cardiac cycle in the spinal canal is approximately 0.9 ml (black line). **b** Detail b shows the volumetric blood flow rate for the arterial (upper red curve), arteriole (red dashed curve), capillary (blue curve), and the venous system (magenta curve). Frame c plots the intracranial pressure waveforms predicted by the model. Red lines represent blood pressures. The green line is the parenchymal pressure which is close to the ventricular, cerebral and spinal subarachnoid ICP. **d** Detail d displays the time dependent pressures for the ventricular system (dark blue), subarachnoid space (light blue), and the spinal canal (dashed) (color in online)

$$p_{init}(t) = c_0 \left[ 1 + \sum_{k=1}^8 a_k \cos(\omega t) + \sum_{k=1}^8 b_k \sin(\omega t) \right], \quad \omega = 2k\pi, \quad k = 1, 2, \dots, 8 \quad (1)$$

The venous pressure signal, labeled  $p_{out}$  was assumed to be flat compared to the arterial signal with 3 mmHg absolute value and zero amplitude, see Appendix, Eqs. (A55)–(A57). The effects of gravity or body activity on the venous and ICP were neglected. Additional interior input conditions include the constant CSF production from the arterioles to the ventricles through the choroid plexus and the diffuse capillary production through the brain parenchyma to the ventricles.

We formulated mass and momentum balances to mathematically describe the flow of blood and CSF and its interaction with the bi-phasic brain compartments. The spatial dimensions were discretized to obtain 84 differential equations with 84 unknown deformations, coupled pressures and flows between the interacting blood, CSF and brain parenchyma. The model has three types of variables for each fluid compartment: the pressure at the center,  $p$ , inflow and efflux,  $f_{in} f_{out}$ , as well as the hydraulic

cross-sectional area,  $A$ . The equations for the right and left brain hemisphere can be adjusted for symmetry or alternatively account for unilateral differences such as Bering's one-sided hydrocephalic experiments on dogs (Bering 1962). Time integration was implemented by a fully implicit Euler scheme. The fully discretized algebraic system was solved numerically using a globally convergent step-size controlled Newton-Raphson method. Details of the numerical techniques can be found elsewhere, (Linninger et al. 2007; Zhang et al. 2007). Flow through each arterial, venous, or CSF compartment is governed by three basic balances: continuity, momentum and distensibility which are described next.

## 2.4 The continuity equation

Continuity ensures that fluid is neither gained nor lost, consistent with the assumption of incompressible blood and CSF flow. The continuity equations can be written as in Eq. (2),

$$l \frac{\partial A}{\partial t} = f_{\text{in}} - f_{\text{out}} + S_{\text{I} \rightarrow \text{II}} \quad (2)$$

where  $l$  is the hydraulic length of the compartment,  $\frac{\partial A}{\partial t}$  is the change in cross-sectional area with respect to time,  $f_{\text{in}}$  and  $f_{\text{out}}$  are the volumetric flow rates in and out of the compartment, respectively. The source or sink terms,  $S_{\text{I} \rightarrow \text{II}}$  account for mass transfer between different compartments as described next.

## 2.5 Fluid exchange between compartments

In addition, some fluid compartments also have permeable boundaries allowing fluid exchange with another phase. For example, CSF production involves mass exchange,  $S_{\text{I} \rightarrow \text{II}}$ , transferring blood plasma from the choroid plexuses into the ventricles,  $S_{\text{AI} \rightarrow \text{LV}}$ . A second source of CSF production occurs throughout the brain parenchyma, which is accounted for by a constant CSF production from the brain capillaries into the extracellular space of the parenchyma,  $S_{\text{constCp} \rightarrow \text{brain}}$ . This diffusely produced CSF may also further seep from the extracellular space of the parenchyma into the ventricles,  $S_{\text{brain} \rightarrow \text{LV}}$ . Seepage from the capillary bed,  $S_{\text{Cp} \rightarrow \text{brain}}$  may occur in both directions depending on the net Starling pressure difference between the capillary pressure and the surrounding brain, (Starling 1896). The specific equations for mass transfer between phases,  $S_{\text{I} \rightarrow \text{II}}$ , are given in the sections for vasculature, CSF and parenchyma, and are also listed in the Appendix Eqs. (A7), (A10), (A24).

## 2.6 Pressure drops

Our model uses a simplified axial momentum balance similar to the Hagen-Poiseuille law.

$$p_{\text{in}} - p = \Delta p = a f_{\text{in}} \quad \text{with } a = 8\pi \mu l / A^2 \quad (3)$$



**Table 2** Physical parameters and their source for cerebral compartments of the intracranial dynamic model

Location	Elastance (Pa)	Volume at rest (cc)
Arteries, Ar	$27.3 \times 10^4$ (Zagzoule and Marc-Vergnes 1986)	30.0 (Zagzoule and Marc-Vergnes 1986)
Arterioles, Al	$40.0 \times 10^4$ (Zagzoule and Marc-Vergnes 1986)	16.0 (Zagzoule and Marc-Vergnes 1986)
Capillaries, Cp	$44.0 \times 10^4$ (Zagzoule and Marc-Vergnes 1986)	20.0 (Zagzoule and Marc-Vergnes 1986)
Veinules, Vl	$117.0 \times 10^4$ (Zagzoule and Marc-Vergnes 1986)	70–80 (Zagzoule and Marc-Vergnes 1986)
Veins, V	$(5.0 - 27.3) \times 10^4$ (Zagzoule and Marc-Vergnes 1986)	
Venous sinus, vSinus	$2.6 \times 10^4$ (Zagzoule and Marc-Vergnes 1986)	13 (Zagzoule and Marc-Vergnes 1986)
Ventricles, Lv	$(0.1 - 1.0) \times 10^4$ (Smillie et al. 2005; Kaczmarek et al. 1997)	15–20 (Lakin et al. 2003; Gjerris and Borgensen 1992)
Cerebral SAS, SAS	$8.0 \times 10^4$ (estimated)	30 (Fishman 1980)
Spinal SAS, sp. canal	$1.0 \times 10^6$ (Wilcox et al. 2003; Bertram et al. 2005)	90–100 (Fishman 1980)
Brain parenchyma	$(1.0 - 10.0) \times 10^3$ (Smillie et al. 2005; Kaczmarek et al. 1997)	1,400 (Fishman 1980)

$p_{in}$  is the pressure of the upstream compartment and  $p$  is the pressure of the current compartment. The term  $a$  is a flow resistance term that accounts for the pressure drop in the fluid along the length of the compartment due to viscous forces; it is a function of the dynamic fluid viscosity,  $\mu$ , the hydraulic length of the compartment,  $l$ , and square of the compartment’s cross-sectional area,  $A$ . The momentum equation relates the pressure drop,  $\Delta p$ , to volumetric flow rate,  $f_{in}$ . Positive  $\Delta p$  along the vessel’s axis causes flow into a compartment, otherwise the flow occurs in the opposite direction. For a thinner vessel, the flow resistance  $a$  increases and a larger pressure drop would be necessary to maintain the same flow rate.

### 2.7 Compartment expansion or compression

The cerebral vasculature, made up of arteries, arterioles, capillaries, veinules, and veins has varying degrees of distensibility. Arteries that surround the brain are typically more compliant than vessels deeply embedded within the brain tissue. We therefore have assigned different values of elastance to each of the cerebral vasculature compartments; these values are given in Table 2 taken from literature. Fluid traction of blood or CSF flow may deform the distensible vascular vessels or CSF compartments. Distensibility of the cerebral vasculature and CSF spaces is incorporated using the steady state force balances implemented in Eq. (4).

$$p_{lumen} - p_{brain} = E \left( \frac{A - A_0}{A_0} \right) \tag{4}$$

The change in a vessel's cross-sectional area,  $A - A_0$ , is governed by the vessel's elastance,  $E$ , and the pressure difference between the vessel lumen and the bi-phasic brain compartment,  $p_{\text{lumen}} - p_{\text{brain}}$ .  $A_0$  is the cross-sectional area at zero transmural pressure (Luo and Pedley 1998). The greater the transmural pressure across the vessel wall, the more expansion or constriction of the vessel will occur. When the blood pressure exceeds the ICP of the surrounding brain tissue, the vessel dilates. Conversely, the vessel may be compressed when the ICP outside is higher. This simple linear distensibility model does not properly describe complex non-linear phenomena like collapsible vessels described by Luo and Pedley (1998) and also neglects auto-regulation. Nevertheless, it fully couples the blood and CSF flow equations with the intracranial brain parenchyma pressure by accounting for: (i) vessel distensibility and brain compliance as a function of the elastance, (ii) effect of vessel expansion on the bi-phasic brain parenchyma (change in brain parenchyma volume and porosity) and (iii) pressure increase of the brain parenchyma due to the effect of vessels' interaction with the parenchyma. It also incorporates the possibility of changes in blood distribution patterns in response to vessel dilation or compression, which in turn follows from the force interactions between the blood and the soft deformable brain tissue as well as coupling with the continuity and axial momentum balances. The specific network connectivity for vasculature, CSF filled spaces and brain parenchyma is discussed next.

## 2.8 Cerebral vasculature

Blood flow exiting the carotid artery, cAr, bifurcates into the cerebral arteries for the right and left brain hemisphere, Ar. The blood then flows into the arterioles, Al. Choroid CSF production diverts plasma from the choroidal blood to generate newly produced CSF in the lateral ventricles, Lv. The choroidal CSF production accounts for about two-thirds of the total CSF production and was found clinically to be almost invariant to pressure changes suggesting an active transport process (Kaczmarek et al. 1997). Accordingly, the mass transfer is a pressure independent constant equal to,  $S_{\text{Al} \rightarrow \text{Lv}} = 0.35 \text{ ml/min}$ . Blood further flows into the capillary bed, where there is also CSF mass transfer from the capillary bed into the parenchyma. This diffuse CSF production rate is  $S_{\text{const Cp} \rightarrow \text{brain}} = 0.12 \text{ ml/min}$ . Moreover, the model accounts for CSF *seepage* allowing capillaries to reabsorb excess fluid or discharge plasma when the interstitial pressure is lowered. The seepage model is governed by the Starling pressure difference which accounts for hydrostatic as well as osmotic pressure differences. Because our model does not balance ions, the effective Starling pressure for fluid seepage is reduced to the hydrostatic pressure difference between capillaries and surrounding brain tissue (Starling 1896). Hence, extracellular fluid reabsorption into the capillaries may occur when ICP rises relative to the capillary pressure. All equations for the mass transfer coupling between blood and CSF are given in the appendix Eqs. (A7), (A10) and (A24). Blood exiting the capillary bed is collected by the veinules, Vl. Again, flows and pressure drops obey to Eqs. (A17), (A20) and (A50). Veinules lead into the large cerebral veins, V, which in turn discharge into the venous sinus, vSinus. Finally, the venous sinus drains into the jugular vein, JV, according to Eq. (A21).

## 2.9 Cerebrospinal fluid (CSF) system

Similar to blood flow, CSF flow in the ventricles and the subarachnoid spaces satisfies continuity, axial momentum and distensibility equations. CSF production is integrated with the cerebral vasculature as described above. Two-thirds are produced in the choroid plexuses, while one-third of CSF has its origin in the distributed capillary bed generating CSF at a constant rate. This diffuse CSF may travel through the parenchyma into ventricles, or traverse the pia to reach the cerebral subarachnoid space. The distribution of the diffusely produced CSF depends on the pressure gradients between the compartments according to the laws of fluid flow in porous media known as Darcy's law. The pressure dependent fluxes are depicted as mass transfer flows,  $S_{\text{CP} \rightarrow \text{brain}}$  and  $S_{\text{brain} \rightarrow \text{Lv}}$ , in Fig. 2 with mathematical expressions for the CSF exchanges in Eqs. (A10), (A24), (A40), (A41), (A44), (A48) and (A51).

The CSF exiting the lateral ventricles, Lv, enters the third ventricle, 3V. CSF from the third ventricle flows through the fourth ventricle, 4V, into the cerebral subarachnoid space, SAS. From the cerebral subarachnoid space, CSF is believed to be reabsorbed into the venous sinus through the arachnoid granulations (DelBigio and Bruni 1988; Segal 2001). We account for CSF reabsorption by a mass transfer flux  $f_{\text{reabsorption}}$ , which is a function of the pressure difference between the subarachnoid space and the venous sinus,  $p_{\text{SAS}} - p_{\text{v.si}}$  and a reabsorption constant,  $k$ , according to Eq. (5). The significance of reabsorption for hydrocephalus will be discussed later.

$$f_{\text{reabsorption}} = k(p_{\text{SAS}} - p_{\text{v.si}}) \quad (5)$$

In addition, CSF may be displaced into the spinal canal. Previous MRI measurements (Loth et al. 2001) have shown that in normal subjects about 0.5–2cc of CSF are displaced from the cranial cavity into the spinal canal and back in every cardiac cycle. These measurements also confirm that the net CSF exchange is zero, thus indicating that the CSF reabsorption in the spinal canal is negligible. Thus, we set the CSF outflow,  $f_{\text{out}}$ , in the continuity equation for the spinal canal to zero. For the displacement to occur, the spinal subarachnoid space must be distensible. This expandability does not violate the Monro-Kellie doctrine because the CSF in the spinal canal is not confined by the cranial vault. The spinal canal compliance is largest in the lumbar area. Moreover, a detailed finite element analysis of the spinal canal expansion in response to CSF influx showed a hyperlinear increase of stiffness with large deformation (Sweetman 2007). Accordingly, we accounted for the nonlinear deformation of the spinal canal in Eqs. (A35)–(A37) and (A38). The momentum equations describing the flow into the spinal canal and venous sinus from the SAS are Eqs. (A50) and (A54).

## 2.10 Brain parenchyma

The brain is a bi-phasic, anisotropic, three-dimensional structure. The Biot-theory of consolidation describes stresses, strains and fluid motion in a consolidating porous media. However, current three-dimensional brain consolidation models with full fluid-structure interaction in addition to the cerebral vasculature and CSF spaces are

still computationally intractable. Therefore, we captured the main dynamic properties without performing a three-dimensional spatial discretization of the brain parenchyma. The brain is merely divided in left and right hemispheres, each one modeled by a single lumped compartment. In the proposed simplified bi-phasic brain model, each hemisphere is treated as an incompressible, deformable medium composed of two phases, the solid cell matrix, representing neurons, glial cells, and axon fibers, and the extracellular fluid. The solid phase normally occupies 70% of its total size. The model assumes that the volume of the solid cell matrix does not change. Thus, size changes of the parenchyma can occur only when extracellular fluid content is altered.

The extracellular fluid content of each brain hemisphere consists of fluid similar to CSF. It occupies 30% of the parenchyma volume and was considered as a viscous and incompressible fluid. The continuity and pressure driven fluid exchange of the bi-phasic brain are given in Eqs. (6)–(8).

Continuity for the extracellular fluid for each brain hemisphere

$$l_{\text{exf}} \frac{\partial A_{\text{exf}}}{\partial t} = f_{\text{exf in}} - f_{\text{exf out}}, \quad (6)$$

Fluid exchange in each hemisphere according to pressure difference

$$\begin{aligned} p_{\text{Cp}} - p_{\text{exf br hem}} &= a_{\text{exf}} S_{\text{Cp} \rightarrow \text{br}}, & \text{with } a_{\text{exf}} &= \mu_{\text{exf}} l_{\text{exf}} / k_{\text{exf}}, \\ p_{\text{exf br hem}} - p_{\text{Lv}} &= a_{\text{exf}} S_{\text{br} \rightarrow \text{Lv}}, \end{aligned} \quad (7)$$

Volume consistency—*Monro-Kellie doctrine*

$$\begin{aligned} V_{\text{total br hem}} &= \sum_b V_b + \sum_{\text{CSF}} V_{\text{CSF}} + V_{\text{br hem}} = \text{constant}, \\ V_{\text{br hem}} &= V_{\text{exf br}} + V_{\text{solid br}}. \end{aligned} \quad (8)$$

The subscript, exf, refers to the extracellular fluid flow inside the left and right brain hemispheres. Each brain hemisphere is modeled as a cylinder with cross-sectional area,  $A_{\text{exf}}$ , and equivalent hydraulic length,  $l_{\text{exf}}$ . The SAS interacts with the two brain hemispheres. The third and fourth ventricles are shared by both hemispheres as shown in Fig. 2. Each brain hemisphere contains arteries, arterioles, capillaries, veinules, veins, and also encases the lateral ventricles. The pressure difference,  $p_{\text{Cp}} - p_{\text{exf br hem}}$ , in Eq. (7) drives seepage of extracellular fluid flow from capillaries into the brain,  $S_{\text{Cp} \rightarrow \text{br}}$ . The term  $p_{\text{exf br hem}} - p_{\text{Lv}}$  in Eq. (7) accounts for the extracellular fluid flow from the brain into the ventricles,  $S_{\text{br} \rightarrow \text{Lv}}$ . The parameter  $a_{\text{exf}}$  is a function of the extracellular fluid viscosity,  $\mu_{\text{exf}}$ , the hydraulic length of the brain hemisphere,  $l_{\text{exf}}$ , and the brain parenchyma permeability,  $k_{\text{exf}}$ , (Biot 1941, 1955; Nield and Bejan 1999). This pressure driven flow can be considered a simplified version of Darcy's law with the hydraulic permeability of the brain parenchyma,  $k_{\text{exf}}$ , given in Table 3, brain parenchyma: Eqs. (A39)–(A44). The pressure difference between the brain,  $p_{\text{exf br hem}}$ , and the surrounding compartments,  $p_b$ ,  $p_{\text{CSF}}$ , *fully couples the brain parenchyma with the cerebral blood and CSF compartments.*

**Table 3** Material properties for the bi-phasic model of intracranial dynamics

Location	Material property	Value/reference
Brain parenchyma	Porosity, $\phi$	0.3 (Lakin et al. 2003)
	Permeability, $k_{\text{exf}}(\text{m}^2)$	$0.7 \times 10^{-15}$ (Lakin et al. 2003)
	Density, $\rho_{\text{exf}}(\text{kg}/\text{m}^3)$	1050 (Pellicer et al. 2006)
	Viscosity, $\mu_{\text{exf}}(\text{kg}/\text{m per s})$	0.001
Blood	density, $\rho_b(\text{kg}/\text{m}^3)$	1050 (Pedley 1980)
	Viscosity, $\mu_b(\text{kg}/\text{m per s})$	0.004 (Pedley 1980)
CSF	Density, $\rho_{\text{CSF}}(\text{kg}/\text{m}^3)$	998.2 (Lakin et al. 2003)
	Viscosity, $\mu_{\text{CSF}}(\text{kg}/\text{m per s})$	0.001 (Lakin et al. 2003)
CSF production	Choroid plexus, $S_{\text{Al} \rightarrow \text{Lv}}$ , (ml/min)	0.35 (Linninger et al. 2005)
	Capillaries diffuse prod., $S_{\text{Cp} \rightarrow \text{br}} + S_{\text{constCp} \rightarrow \text{br}}$ , (ml/min)	0.12 (estimated)
Reabsorption @ sagittal sinus	Permeability, $k$ , ( $\text{m}^2$ )	$N : 0.5 \times 10^{-14}$ $HC : 0.1 \times 10^{-14}$
	Reabsorption, $R$ , (mmHg/ml per min)	$N : 16.0$ (Czosnyka et al. 2004; Gjerris and Borgensen 1992; Kosteljanetz 1989) $HC:88.9$
	Porosity, $\phi$	0.3 (Lakin et al. 2003)
	Max/min (ml/min)	1194/588 <sup>a</sup> (Baledent et al. 2001; Kim et al. 2007)
Venous flow	Max/min ( ml/min)	882/630 <sup>a</sup> (Kim et al. 2007)
Cerebral blood flow	Mean (ml/min)	738
Phase lag	% Cardiac cycle	Predicted 13%/12% in (Kim et al. 2007)

Predicted amplitudes and phase lag for the arterial and venous systems agree with MRI measurements (Kim et al. 2007)

$N$  normal,  $HC$  hydrocephalic

<sup>a</sup> Model predictions

The model also satisfies the Monro-Kellie doctrine stating that total of volumes of all parenchyma, blood and CSF compartments remain constant for each brain hemisphere. The volume consistency of the brain parenchyma and all fluid spaces was enforced through Eq. (8), for each brain hemisphere, Appendix Eq. (A42). In Eq. (8) the volume of the brain parenchyma,  $V_{\text{br\_hem}}$ , is the sum of the volume of extracellular fluid,  $V_{\text{exf\_br}}$ , and the volume of the solid part of the brain,  $V_{\text{solid\_br}}$ . As a result, expansion of the ventricles is only possible when other compartments compress. In principle, volume conservation gives rise to the following options for spatial redistribution: (i) Reduced CSF spaces by displacing CSF into the spinal canal, which is not limited by the cranial *Monro-Kellie doctrine*; (ii) Compression of the brain parenchyma by diminished extracellular fluid content; (iii) Compression of the cerebral vascular bed, which is however expected to influence the cerebral

blood flow. The mathematical analysis will provide quantitative results about the forces and conditions likely to occur in normal and diseased states. The fluid content change relates the volume of the extracellular fluid to the invariant cell matrix of constant volume. This relation is expressed through the brain porosity,  $\phi$ , shown in Eq. (9).

Change to the porosity,  $\phi$  of bi-phasic brain hemisphere

$$\phi_{\text{br\_hem}} = \frac{V_{\text{exf\_br}}}{V_{\text{exf\_br}} + V_{\text{solid\_br}}} = \frac{V_{\text{exf\_br}}}{V_{\text{br\_hem}}}, \quad \text{initial } \phi_{\text{br\_hem}_0} = 0.3. \quad (9)$$

Eq. (9) is applied for each brain hemisphere, Appendix Eq. (A58). A complete description of the equations for each bi-phasic brain compartment and the coupled blood and CSF equations is given in the Appendix. This brain model does not resolve spatial distribution of stresses and strains of the brain. Nevertheless, due to its full coupling with the embedded CSF and blood force and mass balances, it conserves the main features of the porous brain matrix and the induced fluid changes that occur in intracranial dynamics.

### 3 Results

This section introduces the results of the computer predictions for the interactions of all cerebral compartments. The emphasis lies on comparing the differences between normal and hydrocephalic cases to highlight pathological changes and offer to mechanistic explanations.

#### 3.1 Blood and CSF flow dynamics

The predicted blood and CSF flows in normal subjects are depicted in Fig. 3a and b. The total cerebral flow through arteries, arterioles, capillaries and veins, has a mean flow rate of 12.3 ml/s, or 738 ml/min, which is consistent with physiological values (Zagzoule and Marc-Vergnes 1986). The maximum arterial pulsatile flow rate is 19.9 ml/s and the minimum is 9.8 ml/s, matching similar findings to those in (Baledent et al. 2001). The maximum venous pulsatile flow rate is 14.7 ml/s and the minimum is 10.5 ml/s. The pulsatility index (PI) as defined in (Gosling and King 1974) and given in Eq. (10) was calculated and found to be 0.82 in the arteries and 0.34 in the venous system. These pulsatility indices agree with clinically reported measurements (Kim et al. 2007).

$$\text{Pulsatility index} = \frac{\text{maximum systolic flow rate} - \text{minimum diastolic flow rate}}{\text{mean flow rate}} \quad (10)$$

Figure 3a also shows the forward/backward CSF flow of approximately 0.9 cc from the cranium into the spinal canal,  $F_{\text{sp. canal}}$ . The predicted CSF displacement agrees with previous published experimental results based on Cine phase-contrast MRI

(Loth et al. 2001). The CSF stroke-volume into the spinal canal was also predicted for hydrocephalic cases. In hydrocephalus, our model predicts a diminished CSF fluid exchange with the spinal canal. The net forward flux in the hydrocephalic case is only 0.25 ml with each cardiac cycle, *indicating a reduction of 72% of the CSF pulsatility in the cervical area*. Our Cine MRI measurements of CSF flow velocities also showed a reduction of CSF flow in the cervical area in hydrocephalus (Fig. 4).

### 3.2 Hemodynamics

Figure 3c plots predicted blood pressures and pulse waveforms in the normal human brain. The mean pressure in arteries is 82 mmHg, in the arterioles is 55 mmHg, in capillaries is 18 mmHg and drops to 5 mmHg in the veins. Normally, the mean pressure in the brain parenchyma is slightly above the ventricular ICP. Figure 3d shows the simulated ICP signals of the lateral ventricles, cerebral and spinal subarachnoid spaces, for one cardiac cycle. In the ventricles, cerebral and spinal subarachnoid spaces, the pressure has a mean value of 9.1 mmHg. The model predicts approximately 5 mmHg pulse pressure in the ventricular system. This value compares well to a range of 3–5 mmHg reported in Czosnyka et al. (2005). The pulse pressure in the subarachnoid space and spinal canal was computed to be about 3.5 mmHg. The computer predictions also show that the pressure and flow amplitudes of the cerebral veins are attenuated. Our model links this dampening to the dilation of the compliant cerebral vascular bed made possible by CSF displacement into the spinal canal. We note that without the CSF displacement into the spinal canal, the vasculature could not deform the nearly incompressible parenchyma. In addition, the model predicts a phase lag between the arterial and the venous wave forms in the order of 13% of the cardiac cycle as depicted in Fig. 3b. The dampening of the cerebral hemodynamics is clinically well established; our model prediction is in excellent agreement with previous gated MRI blood flow measurements yielding a phase lag of 12% (Kim et al. 2007).

### 3.3 Ratio of aqueduct flow to prepontine flow

The detailed analysis of MRI measurements of CSF flow in normal and hydrocephalic brains shows substantial changes in the flow patterns. Figure 4 shows the computational fluid dynamics simulations and clinical MRI measurements, based on six normal and five communicating hydrocephalic subjects (Linninger et al. 2007, 2005). Compared in detail are the CSF flows in two regions of interest - in the aqueduct of Sylvius and in the prepontine area. In normal subjects, the flow velocity amplitude is much higher in the prepontine area than in the aqueduct. In hydrocephalus, the aqueduct flow is *increased*, while the velocity in the prepontine area is *reduced*. The ratio of the aqueduct to the prepontine velocity amplitude is about seven times larger in hydrocephalic cases than in normals. This change suggests that the *ratio of the prepontine to the aqueduct flow amplitude could be an indicator for the status of communicating hydrocephalus*. While this ratio has not been used for diagnosis yet, its significance might be confirmed in future research. Figure 5 shows snapshots of simulated

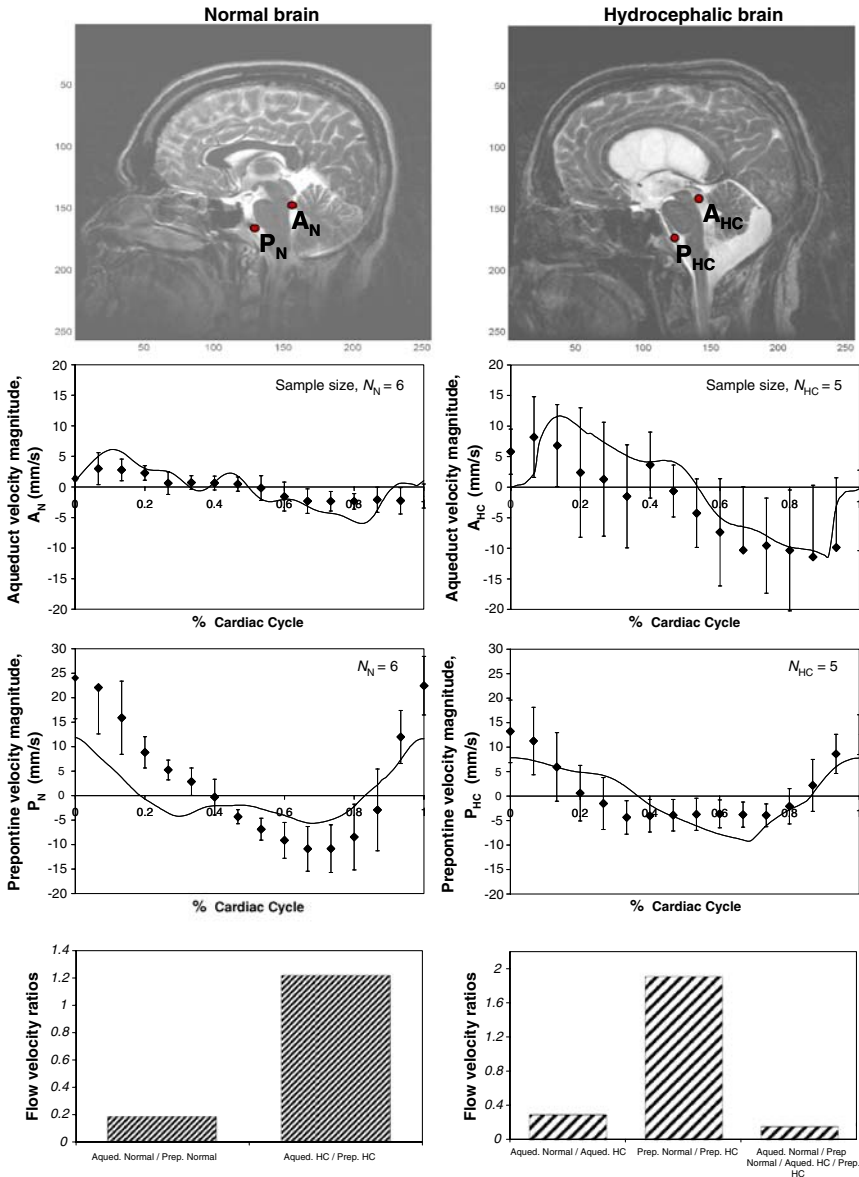


**Fig. 4** In normal brains the average peak to peak velocity at the aqueduct of Sylvius is 6.9 mm/s. In the hydrocephalic case, the amplitude is 3.4 times higher with peak to peak velocity 23.56 mm/s. At the same time the velocity amplitude in the prepontine area is decreased in hydrocephalus. The peak to peak velocity in the prepontine area is about 37 mm/s in normal cases and 19 mm/s in hydrocephalic cases. Velocity measurements based on six normal and five hydrocephalic subjects are shown in *dots*, computer predictions are shown in *solid lines*

velocity fields at the peak of the systole using patient-specific lateral brain sections of a normal and a hydrocephalic subject, where a two dimensional simulation of the flow field is created as previously published (Linninger et al. 2007). The discussion will



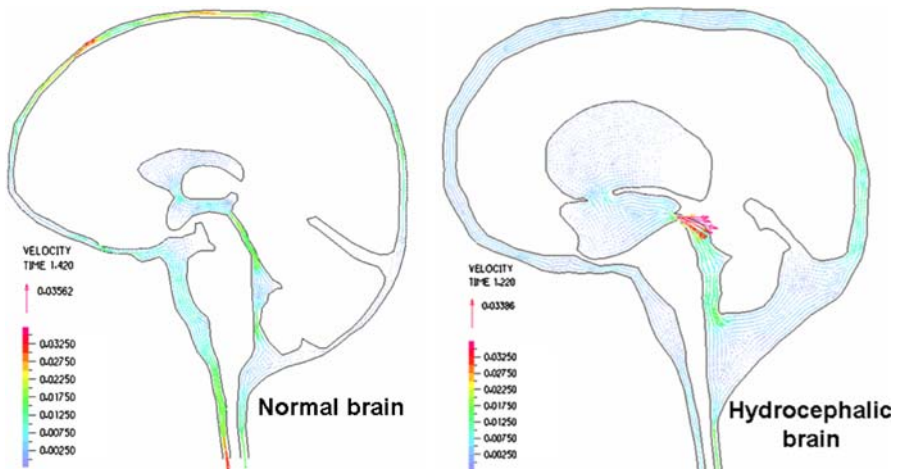


**Fig. 5** Two-dimensional simulation of the CSF flow field at mid systole in a sagittal brain section of normal (*left*) and hydrocephalic subjects (*right*)

present a mechanistic explanation for these changes in the flow patterns occurring in hydrocephalus.

### 3.4 Pulsatile dilation of the lateral ventricles for normal subjects and hydrocephalic patients

The MRI technique described in the methods section was also used to demonstrate the timing for the expansion and contraction of the ventricles in normal and hydrocephalic subjects. When the flow in the lateral ventricles is from superior to inferior, meaning flow from the ventricular system to the cerebral and spinal subarachnoid spaces, the ventricles contract as shown in Fig. 6. When CSF streams upwards from the spinal subarachnoid spaces, then the ventricles expand. We have recently discussed the role of the choroid plexus in driving the CSF flow in the ventricular system (Linninger et al. 2005). In systole, when the fluid space inside the lateral ventricle is compressed, there is outwards CSF flow because the space available for the CSF inside the lateral ventricle is simultaneously confined by the parenchyma as well as by the expanding choroid plexus. Figure 6 compares the percent area change from the MRI measurements with the computational predictions. Since the MRI ventricular size calculation is based on only a single slice, the timing of the wall movement and its relative magnitude (not the absolute amount of fluid moved) can be derived. Note that the model predicts that with hydrocephalus and larger ventricles, the percent movement of the wall is less. Calculation of the total fluid force out of the ventricle cannot yet be done because the detailed geometry of the whole ventricular system is not included.

### 3.5 Transmantle pressure differences

Flow reversal in the aqueduct of Sylvius requires a sign change of the pressure gradients along a streamline. The ventricular space has a higher pressure when CSF is

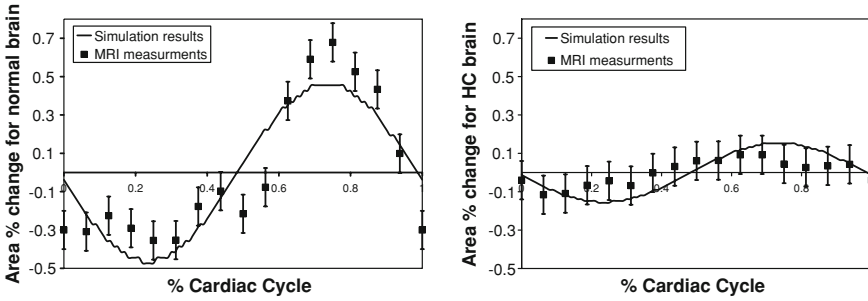


**Fig. 6** Area change for normal and hydrocephalic subjects. Comparison of the MRI area measurements with the simulated results from the computational model

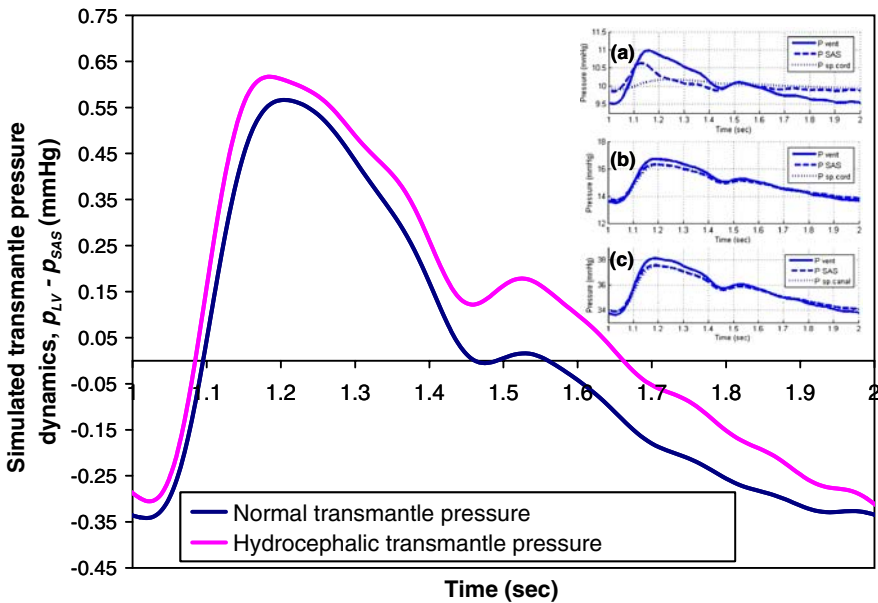


**Fig. 7** Intracranial pressure signals in (a) normal conditions for an individual with carotid blood pressure of 120/90 mmHg, (b) transient phase and (c) fully developed communicating hydrocephalus. The simulations support prior experimental measurements in animal models that showed only small transmantle pressure differences occur in communicating hydrocephalus. Moreover, in each cardiac cycle, there is a pressure sign change, indicating a pulsating loading pattern of the parenchyma

flowing through the aqueduct to the subarachnoid space. The subarachnoid space must have the higher pressure when CSF flows from the subarachnoid space back into the ventricles. Accordingly, the transmantle pressure difference—defined as the pressure difference between the ventricles and cerebral subarachnoid space - changes sign. Figure 7 shows the pressures in the ventricular system, cerebral and spinal subarachnoid spaces in three different phases of hydrocephalus. Initially, the absolute ICP is low not exceeding 11 mmHg as in Fig. 7a. As hydrocephalus gradually develops in our simulation, the ICP increases to 15 mmHg in the ventricular and subarachnoid spaces

shown in Fig. 7b. Finally, the ICP reaches 35 mmHg in the diseased steady state as in Fig. 7c. Despite elevated pressure in acute hydrocephalus, the transmantle pressure signal remains almost unchanged as depicted in Fig. 7. The maximum transmantle pressure difference in normals is 0.56 mmHg (75 Pa), while in acute communicating hydrocephalus it does not exceed 0.62 mmHg (83 Pa). Despite the marked ICP rise, transmantle pressure differences hardly change. On average, the pressure is higher at the ventricular side,  $p_{LV} > p_{SAS}$ , but even this type of compression of the parenchyma from the inside is reversed in each cardiac cycle. Accordingly, the parenchyma experiences dynamic load changes, not static pressure differences with a high pressure at the ventricular side,  $p_{LV}$ , opposed to lower pressures at the interface to the subarachnoid space,  $p_{SAS}$ . Overall, the transmantle pressure does not exceed modest values in both normal and hydrocephalic cases.

### 3.6 Communicating hydrocephalus

The model is able to predict the transition from the normal to the acute diseased state. In all disease simulations only the reabsorption constant was reduced according to Eq. (11); all outcomes follow naturally from the dynamic interactions between the three compartments, blood, CSF and brain parenchyma. The dynamic transitions predicted by the model for the induction of acute communicating hydrocephalus can be compared to our dog models. Kaolin injected into dogs' cisterna magna raises the resistance of reabsorption pathways in the subarachnoid villi (Penn et al. 2005). In humans, the increase of the reabsorption resistance may be due to inflammation of meninges. The acute communicating hydrocephalus is simulated by reducing the reabsorption constant between the subarachnoid space and the sagittal sinus as in Eq. (11).

$$f_{\text{reabsorption}} = k(p_1 - p_2), \quad \begin{cases} \text{normal case: } k = 6.4 \times 10^{-12} \frac{\text{m}^3/\text{s}}{\text{Pa}} & \text{or } R = 16.0 \frac{\text{mmHg}}{\text{ml}/\text{min}} \\ \text{hydrocephalic: } k = 1.4 \times 10^{-12} \frac{\text{m}^3/\text{s}}{\text{Pa}} & \text{or } R = 88.9 \frac{\text{mmHg}}{\text{ml}/\text{min}} \end{cases} \quad (11)$$

Where,  $p_1$ , is the pressure in the cerebral subarachnoid space and,  $p_2$ , is the pressure in the venous sinus. Increased reabsorption resistance causes an ICP rise of 25 mmHg, which is about 3,325 Pa above normal as depicted in Fig. 8b. For the same outflow resistance of  $R = 88.9 \text{ mmHg/ml/min}$ , previous researchers found an ICP elevation from normal dynamics of 15–25 mmHg (1,995–3,325-Pa) (Gjerris and Borgensen 1992). Figure 8a also depicts the pressure trajectories of the ventricular system and the brain parenchyma. The ICP of the brain parenchyma follows the ventricular pressure rise in a period of 22 hours. The detail of Fig. 8b indicates sign changes in the transmantle pressure differences confirming our dog experiments and earlier calculations (Penn et al. 2005; Linninger et al. 2005). The model also correctly predicts the increase in intracranial pulse pressure as has been observed experimentally (Czosnyka et al. 2005; Penn et al. 2005).

Figure 8c shows the volume increase for the lateral ventricles and the cerebral subarachnoid space. In this simulation, the ventricular volume grew to 27 ml, an increase of about 150%. The extracellular fluid content in the brain parenchyma is reduced

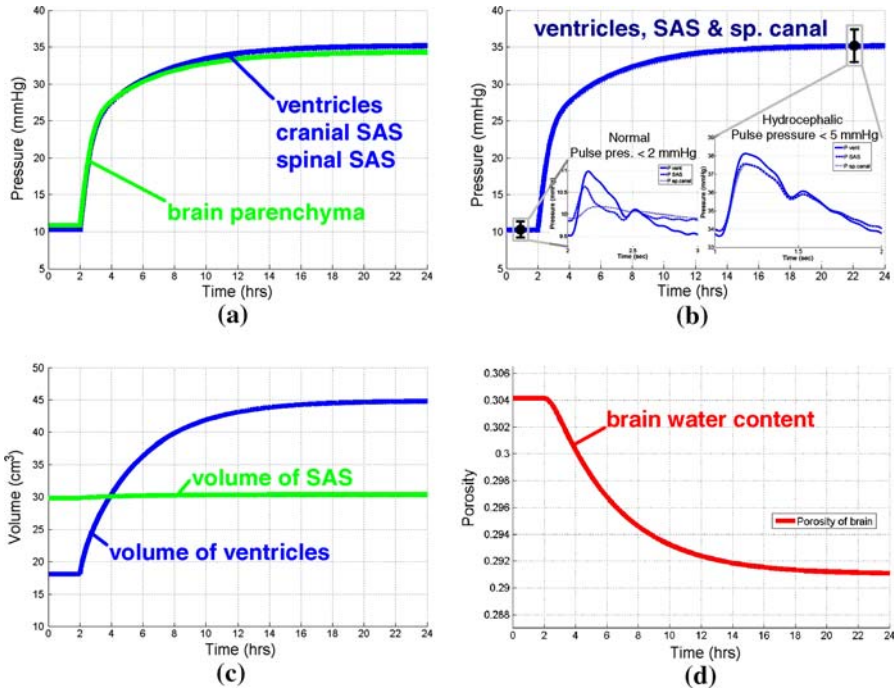


**Fig. 8** Simulated acute communicating hydrocephalus for an individual with carotid blood pressure of 120/90 mmHg. **a** Predicted intracranial pressures for the induction of communicating hydrocephalus. **b** Simulated intracranial pressures and pressure amplitudes for the ventricular system for the induction of communicating hydrocephalus. **c** Volume increase in the ventricular system and cerebral subarachnoid space for the induction of communicating hydrocephalus case. **d** Porosity changes of the brain parenchyma prompted by the onset of simulated acute communicating hydrocephalus

by 25.4 ml. The brain porosity falls from 0.3 to 0.291 or a reduction of about 5% as depicted in Fig. 8d. Figure 9 summarizes the relative expansion and compression of the main cerebral structures and spinal canal occurring in hydrocephalus. The CSF volume increases significantly, and its expansion reduces the extracellular fluid volume in the brain parenchyma. The model also predicts phenomena which are difficult to measure like a small reduction of blood volume which is smallest in the capillaries and larger in the arterial and venous systems.

### 3.7 Clinical infusion tests and the model

Standard clinical methods such as *bolus injections* to determine cerebrospinal compliance in humans permit another test of the model's predictions. The bolus test is done by injecting fluid into the spinal subarachnoid space, while recording the induced pressure rise. The well-known pressure–volume curves provide clinically important information about the brain compliance and are often used for determining treatment options (Czosnyka et al. 2004; Kosteljanetz 1989). If our model is accurate, it should predict compliance curves consistent with clinical observations.

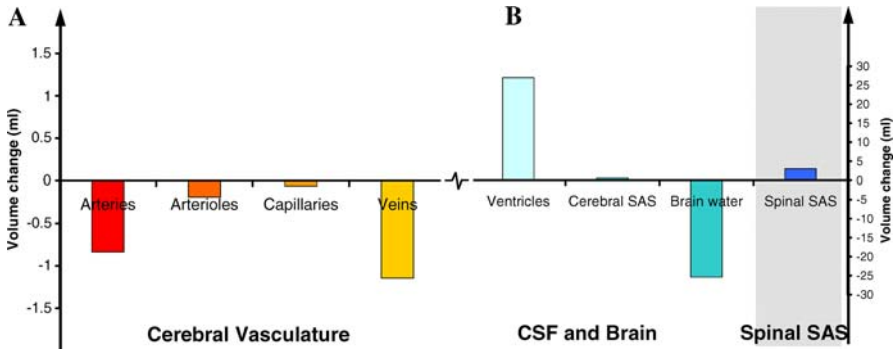


**Fig. 9** The volume change predicted for hydrocephalus relative to normal (baseline) in the vascular and ventricular systems as well as in the brain parenchyma. **a** Volume changes predicted by the model in each vascular substructure of the hydrocephalic human brain in contrast to normal, **b** volume changes of the ventricular system, the brain parenchyma and the spinal canal

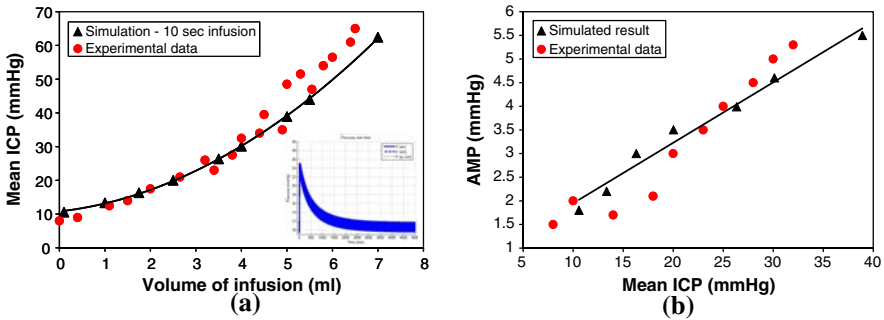


**Fig. 10** Experimental results of bolus injections in humans versus simulated results from the holistic mathematical model, **a** Mean pressure–volume of infusion (P–V) for short time infusion. In the zoomed window on the right lower side the ventricular ICP trajectories after bolus injection in the subarachnoid space are presented. **b** Experimental results versus simulated relationship between pulse amplitude, AMP, and mean ICP for different infusion times

Bolus injections were simulated by inserting a corresponding CSF source in the fluid equations of the subarachnoid space. Dynamic responses of the overall system showed characteristic ICP trajectories with a peak pressure and subsequent relaxation phase as in the detail of Fig. 10a. Figure 10a also shows the typical polynomial relationship between infusion volume and peak pressure. The reported computational trends correlate well with experimental data (Czosnyka et al. 2004). Figure 10b uses the data of the same simulation to correlate pulse amplitude and mean ICP. The pulse amplitude increases with rising ICP with the slope of  $\alpha = 0.128$  in these simulations. Moreover, we calculated the system’s overall mean resistance and found it to be,  $R = 16.0 \text{ mmHg/ml per min}$ . The predicted resistance for the normal brain falls within the range of clinically observed normal reabsorption resistances of 13–18 mmHg/ml per min (Czosnyka et al. 2004).

Using Eq. (12), we also calculated the pressure–volume index (PVI; Czosnyka et al. 2004; Marmarou 1973). We found the PVI for the normal brain to be in the range of

13.5–19 ml. The hydrocephalic brain simulations gave a PVI of 8.0–10.0 ml. These values are below the clinically reported threshold of 13, indicating that our model correctly reproduces the loss of the pressure–volume compensatory reserve (Czosnyka et al. 2004).

$$\text{PVI} = \frac{dV}{\log_{10} \left( \frac{p_p - p_0}{p_b - p_0} \right)}, \quad \left\{ \begin{array}{l} \text{where } p_p : \text{peak pressure} \\ p_b : \text{baseline pressure} \\ p_0 : \text{reference pressure} \end{array} \right. \quad (12)$$

These comparisons demonstrate how clinical measurements can be fit into the model, and how individual patient data can be analyzed to derive specific values for that patient.

## 4 Discussion

We have developed a model for intracranial dynamics in which the interactions of all compartments are quantified by fundamental mass and force conservation balances. Under normal conditions, CSF motion is produced by the vascular expansion and pulsatile brain deformation. Since the parenchyma is incompressible, its deformation is passed on to the ventricles, forcing CSF displacement from the confined cranium into the spinal canal. The Monro-Kellie doctrine is fully satisfied in our model and we have predicted a CSF displacement into the spinal canal of about 0.9 ml in each cardiac cycle. For normal dynamics, the pulsations of the lateral ventricles as well as the amplitudes and pressure gradients of arteries, arterioles, capillaries, veinules and veins can be calculated. It is important to recognize that in simulating communicating hydrocephalus we have simplified the situation for analysis. Firstly, the model does not divide the cerebral subarachnoid space into compartments. Quite likely some forms of hydrocephalus are caused by adsorption blocks at the arachnoid granulations and others by more proximal blocks at the base of the brain. These two situations cannot be distinguished in the current state of the model so the volume changes and pressure in the single cerebral subarachnoid space may be different from what actually occurs. The model, as it stands, predicts that the cerebral subarachnoid space is slightly increased with hydrocephalus. Clinical MRI observations, on the other hand, show a decrease in subarachnoid space in communicating hydrocephalus. MRI measurements need to be quantified in cases of acute hydrocephalus, and our model needs further spatial development to account for changes of the parenchymal cell matrix.

In the current model we have chosen to neglect inertia terms for convenience and to avoid problems that come from wave reflection when using wave equations that include spatial and time derivatives. In the future, the inertia terms should be included, specifically for large arteries in which there are large Womersley numbers. Furthermore, it may be fruitful to divide the vasculature into a more refined network of vessels. The larger arteries and veins are in the cerebral subarachnoid space and the large draining sinuses of the brain may be coupled to the CSF pressure because they share a dural

wall. These possible refinements of the model and their effect on dynamics need to be explored further.

Finally, it needs to be stated clearly that the model only deals with normal brain dynamics and acute onset of hydrocephalus. It does not at this point predict what happens if the developing hydrocephalus changes the brain tissue due to compression or stretching. A number of clinical studies show that plastic changes occur and that hydrocephalus is not perfectly reversible. This is particularly true for the aging brain that no longer has the same physical structure as the adult brain. Some of the non-reversibility of the brain tissue might be due to its porous nature and some due to biochemical/structural changes which take place with deformation. This point was explained in Hakim's original model for normal pressure hydrocephalus over thirty years ago (Hakim et al. 1976).

The lack of reliable measurements of the properties of the brain tissue and CSF absorption also are a problem for all mathematical models. As explained in a recent article on the assessment of CSF outflow resistance, different measurement tests can provide quite different absolute values of  $R_{\text{out}}$  (Eklund et al. 2007). Such measurements all assume that the CSF outflow is linearly dependent on the pressure difference between ICP and the dural sinus, a constant dural sinus pressure and a constant CSF formation rate. They also assume that the only volume change is that of CSF, not blood or spinal subarachnoid space.

While our model has a number of simplifications and is not discretized in three dimensions, it does for the first time couple the three key elements important in intracranial dynamics (the brain, CSF, and blood), and it does so with first principle equations. It provides quantitative explanations for a series of important observations.

#### 4.1 Why does the prepontine fluid flow decrease?

The systolic pulse pressure expands the vasculature producing CSF displacement from the cranium into the spinal subarachnoid space. At normal ICP, the soft tissues in the spinal canal outside the dura can be deformed. However, when the ICP is gradually elevated as in hydrocephalus, the ability of the spinal canal to receive CSF displacements is diminished, thus reducing the system compliance. Impaired compliance explains (i) the reduced CSF flow into spinal canal observable as lower cisternal velocity magnitudes, and (ii) an increase in mean ICP and amplitude reflecting a stiffer cerebrospinal system.

#### 4.2 Why does the aqueduct flow increase simultaneously?

The model suggests that small changes in hemodynamics are responsible. Increased stiffness leads to larger pulse pressures of the cerebral vasculature, which in turn interacts with the bi-phasic parenchyma. At the same time, elevated ICP slightly compresses the cerebral vasculature and drains the parenchyma. Similar compressive trends were reported by previous experimental studies (Czosnyka et al. 2004; Greitz et al. 1994). Compression also impacts the overall blood flow; however, changes in blood flow need to be treated with caution as we did not account for auto-regulation. The

compressed state with larger pulse pressures heightens the pressure and size changes that the ventricles experience. In effect, the forward and backward CSF flows in the lateral and third ventricles are larger in the hydrocephalic case. Therefore, the observable CSF flow in the aqueduct increases. At the same time, cisterna magna flow decreases because of the reduction of the spinal compliance as described above. The proposed mathematical model correctly predicts both aqueduct flow increase and cisterna magna flow decrease using no assumptions other than mass and force conservation balances. While predictions do not prove these points, they offer plausible explanations for the complex changes in flow patterns between cerebral vasculature and CSF compartments occurring in hydrocephalus.

#### 4.3 Transmantle pressure gradients

MRI techniques do not provide absolute ICPs. However, it is possible to accurately reconstruct flows and the necessary pressure differences using the equations of motion together with measured CSF velocities (Linninger et al. 2007; Zhang et al. 2007). These pressure predictions are independent of any assumptions made for the parenchyma. These predictions and actual measurement in dogs confirm that transmantle pressure differences do not cause communicating hydrocephalus as proposed by most previous theories. Previous theories of hydrocephalus (Kaczmarek et al. 1997; Hakim et al. 1976; Smillie et al. 2005) postulating large transmantle pressure gradients are not supported by our model or the evidence of Cine phase-contrast MRI measurements, or by clinical measurements.

#### 4.4 A mechanistic explanation of communicating hydrocephalus

Our model also explains ventricular expansion in the acute onset of communicating hydrocephalus. The model predicts that fluid exchange between the main cerebral compartments occurs in communicating hydrocephalus. Normally, the ventricular system drains CSF from the arteries of the choroid plexus and from the brain parenchyma. CSF is reabsorbed into the venous system at the superior sagittal sinus. Impaired reabsorption causes CSF to accumulate and hydrocephalus to develop. Despite a gradual ICP increase, CSF is continuously produced because CSF production is only a weak function of ICP, perhaps due to active transport mechanisms underlying CSF production (Brown et al. 2004; Segal 2001). Continued CSF production leads to CSF accumulation in the ventricles, at the same time CSF transport from the vascular to the ventricular system through the extracellular space is diminished. Finally, as the ICP further rises, the CSF reabsorption flow is restored, but requires much higher ICP to off-set increased reabsorption resistance. In this final state, only a small amount of CSF is predicted to seep back into the vasculature from the ventricles through the extracellular space, which constitutes a complete reversal of CSF flow direction when compared to the normal state. The ventricles stay enlarged unless treatment restores the original conditions. This explanation of ventricular expansion is consistent with the laws of fluid mechanics and poroelasticity despite the occurrence of only small transmantle pressure differences.



## 5 Conclusions

The model of intracranial dynamics incorporates interactions of all significant intracranial contents including the vascular system, CSF and the parenchyma. It does so for each pulsation of the cardiac cycle or multiple cycles over time. By changing one factor, the resistance to CSF absorption, communicating hydrocephalus and its onset can be simulated. This first principle model has been compared to actual Cine phase-contrast MRI of normal subjects and patients with hydrocephalus and found to properly reflect the observed dynamic flow patterns. To account for the all relevant system interactions, we have included the spinal canal with its more compliant epidural surface compared to the brain. The spinal subarachnoid space is normally very compliant because of the soft tissue and vessels that surrounds the dural face and acts as a cushion. Its deformability permits CSF displacement from the cranium into the spinal canal. Normal pulsations amount to approximately 0.9 ml of flow back and forth through the foramina of magnum with each cycle. At high ICP, compliance decreases as the spinal canal is stretched. Thus, less CSF can be exchanged from the cranium to the spinal canal against a more compressed tissue. Our model incorporates these characteristics and plausibly explains the decrease in the cisternal CSF flow in hydrocephalus.

Some aspects of the mystery of acute communicating hydrocephalus have been explained. The model, however, does not aim to explain chronic forms of hydrocephalus, hemodynamic effects caused by pseudo-tumors or dural sinus thrombosis. Future work will resolve in more detail the cerebral vascular tree to increase the fidelity of the predictions as well as to quantify the effect of brain deformations on the local blood flow, straining or elongation of blood vessels in the periventricular area. More questions about the physiological consequences of the physical changes in its chronic phase arise. How does the brain and vasculature adapt to stretching or compressing, and what specifically causes damage to the brain? Knowing the fundamental physics of the central nervous system provides a scientific understanding of the forces that affect the brain tissue and may help predict when irreversible damage will occur. The same type of physical analysis can be applied to tumors, hemorrhagic strokes and sub-dural hemorrhages, and can potentially lead to a better understanding of these pathological states. Much work remains to be done in expanding the model, but the integration of the major components (blood, CSF, and parenchyma) appears to provide a good start into understanding intracranial dynamics.

**Acknowledgments** The authors gratefully acknowledge partial financial support of this project from NIH Grant 5R21EB004956, a grant from the Stars Kid Foundation, as well as NSF Grant CBET-0756154.

## Appendix

This appendix contains all equations for each compartment of the developed multi-compartment dynamical model of intracranial dynamics.

## First tube equations—carotid artery

$$l_{cAr} \frac{\partial A_{cAr}}{\partial t} = f_{cAr_{in}} - f_{cAr_{out}}, \quad \text{continuity} \quad (\text{A1})$$

$$p_{init} - p_{cAr} = a_{cAr} f_{cAr_{in}}, \quad \text{momentum} \quad (\text{A2})$$

$$p_{cAr} - 0.5 (p_{exf_{br}^L} + p_{exf_{br}^R}) = E_{cAr} \left( \frac{A_{cAr}}{A_{cAr0}} - 1 \right), \quad \text{distensibility} \quad (\text{A3})$$

## First system—vascular system (blood) for left (L) and right (R) hemispheres

## Arteries

$$l_{Ar}^{L,R} \frac{\partial A_{Ar}^{L,R}}{\partial t} = f_{Ar_{in}}^{L,R} - f_{Ar_{out}}^{L,R}, \quad \text{continuity} \quad (\text{A4})$$

$$p_{cAr} - p_{Ar}^{L,R} = a_{Ar}^{L,R} f_{Ar_{in}}^{L,R}, \quad \text{momentum} \quad (\text{A5})$$

$$p_{Ar}^{L,R} - p_{exf_{br}}^{L,R} = E_{Ar} \left( \frac{A_{Ar}^{L,R}}{A_{Ar0}^{L,R}} - 1 \right), \quad \text{distensibility} \quad (\text{A6})$$

## Arterioles

$$l_{Al}^{L,R} \frac{\partial A_{Al}^{L,R}}{\partial t} = f_{Al_{in}}^{L,R} - f_{Al_{out}}^{L,R} + S_{Al \rightarrow Lv}^*, \quad \text{continuity} \quad (\text{A7})$$

$$p_{cAr} - p_{Al}^{L,R} = a_{Al}^{L,R} f_{Al_{in}}^{L,R}, \quad \text{momentum} \quad (\text{A8})$$

$$p_{Al}^{L,R} - p_{exf_{br}}^{L,R} = E_{Al} \left( \frac{A_{Al}^{L,R}}{A_{Al0}^{L,R}} - 1 \right), \quad \text{distensibility} \quad (\text{A9})$$

## Capillaries

$$l_{Cp}^{L,R} \frac{\partial A_{Cp}^{L,R}}{\partial t} + f_{Cp_{out}}^{L,R} - f_{Cp_{in}}^{L,R} = S_{Cp \rightarrow br}^{L,R} + S_{const_{Cp \rightarrow br}}^*, \quad \text{continuity} \quad (\text{A10})$$

$$p_{Al}^{L,R} - p_{Cp}^{L,R} = a_{Cp}^{L,R} f_{Cp_{in}}^{L,R}, \quad \text{momentum} \quad (\text{A11})$$

$$p_{Cp}^{L,R} - p_{exf_{br}}^{L,R} = E_{Cp} \left( \frac{A_{Cp}^{L,R}}{A_{Cp0}^{L,R}} - 1 \right), \quad \text{distensibility} \quad (\text{A12})$$

## Veinules

$$l_{Vl}^{L,R} \frac{\partial A_{Vl}^{L,R}}{\partial t} = f_{Vl_{in}}^{L,R} - f_{Vl_{out}}^{L,R}, \quad \text{continuity} \quad (\text{A13})$$

$$p_{Cp}^{L,R} - p_{Vl}^{L,R} = a_{Vl}^{L,R} f_{Vl_{in}}^{L,R}, \quad \text{momentum} \quad (\text{A14})$$

$$p_{V1}^{L,R} - p_{\text{exf\_br}}^{L,R} = E_{V1} \left( \frac{A_{V1}^{L,R}}{A_{V1_0}^{L,R}} - 1 \right), \quad \text{distensibility} \tag{A15}$$

Veins

$$l_V^{L,R} \frac{\partial A_V^{L,R}}{\partial t} = f_{V_{\text{in}}}^{L,R} - f_{V_{\text{out}}}^{L,R}, \quad \text{continuity} \tag{A16}$$

$$p_{V1}^{L,R} - p_V^{L,R} = a_V^{L,R} f_{V_{\text{in}}}^{L,R}, \quad \text{momentum} \tag{A17}$$

$$p_V^{L,R} - p_{\text{exf\_br}}^{L,R} = E_V \left( \frac{A_V^{L,R}}{A_{V_0}^{L,R}} - 1 \right), \quad \text{distensibility} \tag{A18}$$

Venous sinus

$$l_{v\text{Sinus}} \frac{\partial A_{v\text{Sinus}}}{\partial t} = f_{v\text{Sinus}_{\text{in}}} - f_{v\text{Sinus}_{\text{out}}}, \quad \text{continuity} \tag{A19}$$

$$0.5 (p_{vL} + p_{vR}) - p_{v\text{Sinus}} = a_{v\text{Sinus}} f_{v\text{Sinus}_{\text{in}}}, \quad \text{momentum} \tag{A20}$$

$$p_{v\text{Sinus}} - p_{\text{out}} = a_{v\text{Sinus}} f_{v\text{Sinus}_{\text{out}}}, \quad \text{momentum} \tag{A21}$$

$$p_{v\text{Sinus}} - 0.5 (p_{\text{exf\_br}^L} + p_{\text{exf\_br}^R}) = E_{v\text{Sinus}} \left( \frac{A_{v\text{Sinus}}}{A_{v\text{Sinus}_0}} - 1 \right), \quad \text{distensibility} \tag{A22}$$

\* $S_{\text{Al} \rightarrow \text{Lv}}$  indicates constant production of CSF consistent with known physiological values,  $S_{\text{Cp} \rightarrow \text{br}}^{L,R} + S_{\text{constCp} \rightarrow \text{br}}^{L,R}$  are the diffuse pressure driven and constant productions from capillaries to the brain parenchyma for the left and right brain hemispheres.

Second system—ventricular system (CSF) for left (L) and right (R) hemispheres

Lateral ventricles

$$l_{Lv}^{L,R} \frac{\partial A_{Lv}^{L,R}}{\partial t} = f_{Lv_{\text{in}}}^{L,R} - f_{Lv_{\text{out}}}^{L,R}, \quad \text{continuity} \tag{A23}$$

$$f_{Lv_{\text{in}}}^{L,R} = S_{\text{Al} \rightarrow \text{Lv}} + S_{\text{br} \rightarrow \text{Lv}}^{L,R} + S_{\text{constbr} \rightarrow \text{Lv}}^{L,R} \tag{A24}$$

$$p_{Lv}^{L,R} - p_{\text{exf\_br}}^{L,R} = E_{Lv} \left( \frac{A_{Lv}^{L,R}}{A_{Lv_0}^{L,R}} - 1 \right), \quad \text{distensibility} \tag{A25}$$

Third ventricle

$$l_{3V} \frac{\partial A_{3V}}{\partial t} = f_{3V_{\text{in}}} - f_{3V_{\text{out}}}, \quad \text{continuity} \tag{A26}$$

$$0.5 (p_{Lv^L} + p_{Lv^R}) - p_{3V} = a_{3V} f_{3V_{\text{in}}}, \quad \text{momentum} \tag{A27}$$

$$p_{3V} - 0.5 (p_{\text{exf\_br}^L} + p_{\text{exf\_br}^R}) = E_{3V} \left( \frac{A_{3V}}{A_{3V_0}} - 1 \right), \quad \text{distensibility} \tag{A28}$$

Fourth ventricle

$$l_{4V} \frac{\partial A_{4V}}{\partial t} = f_{4V_{in}} - f_{4V_{out}}, \quad \text{continuity} \tag{A29}$$

$$p_{3V} - p_{4V} = a_{4V} f_{4V_{in}}, \quad \text{momentum} \tag{A30}$$

$$p_{4V} - 0.5(p_{\text{exf}_{br^L}} + p_{\text{exf}_{br^R}}) = E_{4V} \left( \frac{A_{4V}}{A_{4V_0}} - 1 \right), \quad \text{distensibility} \tag{A31}$$

Cranial subarachnoid space

$$l_{SAS} \frac{\partial A_{SAS}}{\partial t} = f_{SAS_{in}} - f_{SAS_{out}}, \quad \text{continuity} \tag{A32}$$

$$p_{4V} - p_{SAS} = a_{SAS} f_{SAS_{in}}, \quad \text{momentum} \tag{A33}$$

$$p_{SAS} - 0.5(p_{\text{exf}_{br^L}} + p_{\text{exf}_{br^R}}) = E_{SAS} \left( \frac{A_{SAS}}{A_{SAS_0}} - 1 \right), \quad \text{distensibility} \tag{A34}$$

Spinal subarachnoid space

$$l_{\text{sp.canal}} \frac{\partial A_{\text{sp.canal}}}{\partial t} = f_{\text{sp.canal}_{in}} - f_{\text{sp.canal}_{out}}, \quad \text{continuity} \tag{A35}$$

$$p_{SAS} - p_{\text{sp.canal}} = a_{\text{sp.canal}} f_{\text{sp.canal}_{in}}, \quad \text{momentum} \tag{A36}$$

$$\begin{aligned} p_{\text{sp.canal}} - 0.5(p_{\text{exf}_{br^L}} + p_{\text{exf}_{br^R}}) \\ = E_{\text{sp.canal}} \left( \frac{A_{\text{sp.canal}}}{A_{\text{sp.canal}_0}} - 1 \right), \quad \text{distensibility} \end{aligned} \tag{A37}$$

$$\begin{aligned} E_{\text{sp.canal}} = a + b\Delta V + c\Delta V^2, \quad \text{where } \Delta V = V - V_0, \text{ and} \\ a = 213312.0, b = 2666.4, c = 399.96 \end{aligned} \tag{A38}$$

\*\*  $S_{br \rightarrow LV}^{L,R}$ ,  $S_{\text{const}_{br \rightarrow LV}}^{L,R}$  are the diffuse pressure driven and constant productions from the brain parenchyma to the lateral ventricles for the left and right brain hemispheres.

Third system—brain parenchyma (Brain), left (L) and right (R) hemispheres

Left and right brain hemispheres

$$l_{br}^{L,R} \frac{\partial A_{br}^{L,R}}{\partial t} = f_{br_{in}}^{L,R} - f_{br_{out}}^{L,R}, \quad \text{continuity} \tag{A39}$$

$$p_{Cp}^{L,R} - p_{\text{exf}_{br}}^{L,R} = a_{\text{exf}}^{L,R} S_{Cp \rightarrow br}^{L,R}, \quad \text{momentum} \tag{A40}$$

$$p_{\text{exf}_{br}}^{L,R} - p_{LV}^{L,R} = a_{\text{exf}}^{L,R} S_{br \rightarrow LV}^{L,R}, \quad \text{momentum} \tag{A41}$$

$$\begin{aligned}
 V_{\text{total\_br\_hem}}^{L,R} &= \text{constant} \\
 \Rightarrow (V_{\text{Ar}}^{L,R} + V_{\text{Al}}^{L,R} + V_{\text{Cp}}^{L,R} + V_{\text{Vl}}^{L,R} + V_{\text{V}}^{L,R} + V_{\text{vSinus}}) \\
 &+ (V_{\text{Lv}}^{L,R} + 0.5V_{\text{3V}} + 0.5V_{\text{4V}} + V_{\text{SAS}}) + V_{\text{br\_hem}}^{L,R} = \text{constant}, \\
 \text{where } V_{\text{br\_hem}}^{L,R} &= V_{\text{exf\_br}}^{L,R} + V_{\text{solid\_br}}^{L,R} = A_{\text{exf\_br}}^{L,R} I_{\text{exf\_br}}^{L,R} + A_{\text{solid\_br}}^{L,R} I_{\text{solid\_br}}^{L,R}, \\
 \text{volume consistency} & \tag{A42}
 \end{aligned}$$

Constant diffuse production equations

$$S_{\text{constCp}\rightarrow\text{br}}^{L,R} = 0.0005\text{ml/s} \tag{A43}$$

$$S_{\text{constbr}\rightarrow\text{Lv}}^{L,R} = 0.0005\text{ml/s} \tag{A44}$$

Equations connecting the compartments and source terms

$$f_{\text{cArout}} = f_{\text{Arin}}^R + f_{\text{Arin}}^L \tag{A45}$$

$$f_{\text{Arout}}^{L,R} = f_{\text{Alin}}^{L,R} \tag{A46}$$

$$f_{\text{Alout}}^{L,R} = f_{\text{Cpin}}^{L,R} + S_{\text{Al}\rightarrow\text{Lv}} \tag{A47}$$

$$f_{\text{Cpout}}^{L,R} = f_{\text{Vlin}}^{L,R} + S_{\text{Cp}\rightarrow\text{br}}^{L,R} + S_{\text{constCp}\rightarrow\text{br}}^{L,R} \tag{A48}$$

$$f_{\text{Vlout}}^{L,R} = f_{\text{Vin}}^{L,R} \tag{A49}$$

$$f_{\text{Vout}}^R + f_{\text{Vout}}^L = f_{\text{vSinusin}} - f_{\text{reabsorption}} \tag{A50}$$

$$f_{\text{Lvout}}^R + f_{\text{Lvout}}^L = f_{\text{3Vin}} + S_{\text{br}\rightarrow\text{Lv}}^L + S_{\text{br}\rightarrow\text{Lv}}^R \tag{A51}$$

$$f_{\text{3Vout}} = f_{\text{4Vin}} \tag{A52}$$

$$f_{\text{4Vout}} = f_{\text{SASin}} \tag{A53}$$

$$f_{\text{SASout}} = f_{\text{reabsorption}} + f_{\text{sp.canalin}} \tag{A54}$$

where  $f_{\text{reabsorption}} = k(p_{\text{SAS}} - p_{\text{vSinus}})$  is a pressure driven flow rate

Boundary conditions

$$p_{\text{init}} = p_{\text{carotid}}, \text{ average pressure } 100\text{ mm Hg, pulsatile,} \tag{A55}$$

$$p_{\text{out}} = p_{\text{venous}}, \text{ absolute pressure } 3\text{ mm Hg, zero amplitude,} \tag{A56}$$

$$f_{\text{sp.canalout}} = 0, \text{ no flow at the end of the spinal canal.} \tag{A57}$$

Equations for evaluating the porosity of the left (L) and right (R) brain hemispheres

$$\phi_{\text{br\_hem}}^{L,R} = \frac{V_{\text{exf\_br}}^{L,R}}{V_{\text{exf\_br}}^{L,R} + V_{\text{solid\_br}}^{L,R}} = \frac{V_{\text{exf\_br}}^{L,R}}{V_{\text{br\_hem}}^{L,R}} \tag{A58}$$

## References

- Baledent O, Henry-Feugeas MC, Idy-Peretti I (2001) Cerebrospinal fluid dynamics and relation with blood flow: a magnetic resonance study with semiautomated cerebrospinal fluid segmentation. *Invest Radiol* 36:368
- Bering EA (1962) Circulation of the cerebrospinal fluid. *J Neurosurg* 19:405
- Bertram CD, Brodbelt AR, Stoodley MA (2005) The origins of syringomyelia: numerical models of fluid/structure interactions in the spinal cord. *J Biomed Eng* 127:1099
- Biot MA (1941) General theory of three-dimensional consolidation. *J Appl Phys* 12:155
- Biot MA (1955) Theory of elasticity and consolidation for a porous anisotropic solid. *J Appl Phys* 26(2):182
- Brown P, Davies S, Speake T, Millar I (2004) Molecular mechanisms of cerebrospinal fluid production. *Neuroscience* 129:957
- Czosnyka Z, Czosnyka M, Richards HK, Pickard JD (2002) Laboratory testing of hydrocephalus shunts—Conclusion of the UK shunt evaluation programme. *Acta Neurochir* 144(6):525
- Czosnyka M, Czosnyka Z, Momjian S, Pickard JD (2004) Cerebrospinal fluid dynamics. *Physiol Meas* 25(5):R51
- Czosnyka Z, Cieslicki K, Czosnyka M, Pickard JD (2005) Hydrocephalus shunts and waves of intracranial pressure. *Med Biol Eng Comput* 43(1):71
- de Boor C (2001) A Practical guide to splines. Springer, New York
- DelBigio MR, Bruni JE (1988) Changes in periventricular vasculature of rabbit brain following induction of hydrocephalus and after shunting. *J Neurosurg* 69:115
- Dumoulin CL, Souza SP, Walker MF, Yoshitome E (1988) Time-resolved magnetic resonance angiography. *Magn Reson Med* 6(3):275
- Eklund A, Smielewski P, Chambers I, Alperin N, Malm J, Czosnyka M, Marmarou A (2007) Assessment of cerebrospinal fluid outflow resistance. *Med Biol Eng Comput* 45:719
- Fishman RA (1980) Cerebrospinal fluid in disease of the nervous system. W.B. Saunders Company, Philadelphia 63–140
- Gjerris F, Borgesen SE (1992) Pathophysiology of cerebrospinal fluid circulation. In: Crockard A, Hayward A, Hoff J (eds) *Neurosurgery: the scientific basis of clinical practice*. Blackwell Scientific, Cambridge, pp 147–168
- Gosling RG, King DH (1974) Arterial assessment by Doppler-shift ultrasound. *Proc R Soc Med* 67:447
- Greitz D, Hannerz J, Rahn T, Bolander H, Ericsson A (1994) MR imaging of cerebrospinal fluid dynamics in health and disease. On the vascular pathogenesis of communicating hydrocephalus and benign intracranial hypertension. *Acta Radiol* 35(3):204
- Hakim S, Venegas JG, Burton JD (1976) The physics of the cranial cavity, hydrocephalus and normal pressure hydrocephalus: mechanical interpretation and mathematical model. *Surg Neurol* 5:187
- Kaczmarek M, Subramaniam RP, Neff SR (1997) The hydromechanics of hydrocephalus: Steady-state solutions for cylindrical geometry. *Bull Math Biol* 59(2):295
- Kim J, Thacker NA, Bromiley PA, Jackson A (2007) Prediction of the jugular venous waveform using a model of CSF dynamics. *Am J Neuroradiol* 28:983
- Kosteljanetz M (1989) Measurement of resistance to outflow: the bolus injection method. In: Gjerris F, Borgesen SE, Sorensen PS (eds) *Proceedings Outflow of cerebrospinal fluid*, pp 134–143
- Lakin WD, Stevens SA, Tranmer BI, Penar PL (2003) A whole-body mathematical model for intracranial pressure dynamics. *J Math Biol* 46(4):347
- Linninger AA, Tsakiris C, Zhu DC, Xenos M, Roycewicz P, Danziger Z, Penn RD (2005) Pulsatile cerebrospinal fluid dynamics in the human brain. *IEEE Trans Biomed Eng* 52(4):557
- Linninger AA, Xenos M, Zhu DC, Somayaji MR, Kondapalli S, Penn RD (2007) Cerebrospinal fluid flow in the normal and hydrocephalic human brain. *IEEE Trans Biomed Eng* 54(2):291
- Loth F, Yardimci AM, Alperin N (2001) Hydrodynamic modeling of cerebrospinal fluid motion within the spinal cavity. *J Biomech Eng* 123(1):71
- Luo XY, Pedley TJ (1998) The effects of wall inertia on flow in a two-dimensional collapsible channel. *J Fluid Mech* 363:253
- Marmarou A (1973) A theoretical model and experimental evaluation of the cerebrospinal fluid system. Thesis, Drexel University, Philadelphia, PA
- Marmarou A, Shulman K, Rosende RM (1978) A nonlinear analysis of the cerebrospinal fluid system and intracranial pressure dynamics. *J Neurosurg* 48:332
- Nield D, Bejan A (1999) *Convection in porous media*. Springer, New York

- Pedley TJ (1980) *The fluid mechanics of large blood vessels*. Cambridge University Press, Cambridge
- Pelc NJ, Bernstein MA, Shimakawa A, Glover GH (1991) Encoding strategies for three-direction phase-contrast MR imaging of flow. *J Magn Reson Imaging* 1(4):405
- Penn RD, Lee MC, Linninger AA, Miesel K, Lu SN, Stylos L (2005) Pressure Gradients in the Brain in an experimental model of hydrocephalus. *J Neurosurg* 102(6):1069
- Pellicer A, Gaya F, Madero R, Quero J, Cabanas F (2006) Noninvasive continuous monitoring of the effect of head position on brain hemodynamics in ventilated infants. *Pediatrics* 109(3):434
- Piechnik SK, Czosnyka M, Harris NG, Minhas PS, Pickard JD (2001) A Model of the Cerebral and Cerebrospinal Fluid Circulations to Examine Asymmetry in Cerebrovascular Reactivity. *J Cereb Blood Flow Metab* 21:182
- Raksin PB, Alperin N, Sivaramakrishnan A, Surapaneni S, Lichtor T (2003) Noninvasive intracranial compliance and pressure based on dynamic magnetic resonance imaging of blood flow and cerebrospinal fluid flow: review of principles, implementation, and other noninvasive approaches. *Neurosurg Focus* 14(4):1
- Segal M (2001) Transport of nutrients across the choroid plexus. *Microsc Res Tech* 52:38
- Smillie A, Sobey I, Molnar Z (2005) A hydroelastic model of hydrocephalus. *J Fluid Mech* 539:417
- Sorek S, Bear J, Karni Z (1988a) A non-steady compartmental flow model of the cerebrovascular system. *J Biomech* 21(9):695
- Sorek S, Feinsod M, Bear J (1988b) Can NPH be caused by cerebral small vessel disease? A new look based on a mathematical model. *Med Biol Eng Comput* 26(3):310
- Sorek S, Bear J, Karni Z (1989) Resistances and compliances of a compartmental model of the cerebrovascular system. *Ann Biomed Eng* 17(1):1
- Starling EH (1896) On the absorption of fluids from the connective tissue spaces. *J Physiol* 19:312
- Stevens S (2000) Mean pressures and flows in the human intracranial system, determined by mathematical simulations of a steady-state infusion test. *Neurol Res* 22(8):809
- Sweetman B (2007) Quantification of intracranial dynamics under normal and hydrocephalic conditions. Thesis, University of Illinois at Chicago, Chicago, IL
- Ursino M, Lodi CA (1997) A simple mathematical model of the interaction between intracranial pressure and cerebral hemodynamics. *J Appl Physiol* 82(4):1256
- Wilcox RK, Bilston LE, Barton DC, Hall RM (2003) Mathematical model for the viscoelastic properties of dura mater. *J Orthop Sci* 8:432
- Zagzoule M, Marc-Vergnes J (1986) A global mathematical model of the cerebral circulation in man. *J Biomech* 19(12):1015
- Zhang L, Kulkarni K, Somayaji MR, Xenos M, Linninger AA (2007) Discovery of transport and reaction properties in distributed systems. *AIChE J* 53(2):381
- Zhu DC, Xenos M, Linninger AA, Penn RD (2006) Dynamics of lateral ventricle and cerebrospinal fluid in normal and hydrocephalic brains. *J Magn Reson Imaging* 24(4):756